SURFACE MODIFICATION METHODS OF ZRICONIUM ALLOY FUEL CLADDING TUBE FOR MITIGATION OF CORROSION PRODUCT DEPOSIT IN SIMULATED PWR PRIMARY COOLANT

H.-S. SHIM and S.-W. KIM
Korea Atomic Energy Research Institute (KAERI)
Daejeon, Republic of Korea
Email: hshim@kaeri.re.kr

1. Introduction

The structural materials of pressurized water reactors(PWRs), which are mainly composed of Ni-Cr-Fe alloys, are slowly corroded in high temperature primary water. Corrosion products formed on the surface of main components such as steam generator, reactor internal, fuel and piping are released into the coolant and then transported into a core. The transported corrosion products are deposited on the fuel cladding tubes and are activated by a neutron flux in the core. These corrosion products are specifically called crud (an acronym for chalk river unidentified deposits). Crud has been known to be composed of mainly Fe, Ni, and Zr oxides in phases of nickel ferrite, nickel oxide, iron oxide, zirconium oxide, and bonaccordite, etc [1-4]. Crud also has a porous structure because it is formed with sub-cooled nucleate boiling (SNB) [3]. In PWRs, pores and chimneys within crud are believed to be developed through the escape of steam formed on the interface between fuel cladding surface and crud towards the cooling water.

Various chemical species in primary coolant can be concentrated in these pores of the crud. Among them, concentrated boron compounds can induce local power distortion due to neutron capture by boron, resulting power output de-rating [1,5]. Furthermore, the crud on fuel cladding can increase its surface temperature due to increased thermal resistance and that results the acceleration of fuel cladding corrosion [6,7]. In addition, the ex-core deposit of activated crud leads an increase in occupational radiation exposure (ORE) of workers during outage [3].

Recently, such crud issues are on the rise due to an extended fuel cycle and a high burn-up operation program [8]. Therefore, several methods have been implemented to plants to mitigate above operational problems caused by crud. Elevated pH operation of the reactor coolant chemistry from 6.0 to 7.2-7.4 results a reduction in crud deposition amount in PWRs [9, 10]. Ultrasonic fuel cleaning has been applied to remove crud from the reloaded fuel assemblies during overhaul [11,12].

The crud deposition on fuel cladding can be accelerated by increase of SNB events and corrosion product concentration in the coolant, and enforcement of adhesion of corrosion product particles onto cladding surface [13,14]. Among them, SNB and surface-corrosion particle interaction have a very close relationship with the surface property of fuel cladding such as roughness, wettability and zeta potential [15-17]. Studies on the effect of surface properties have reported that nucleate boiling occurs actively on a rough surface than on a smooth surface and the departure frequency of steam bubbles increases on a hydrophobic surface than on a hydrophilic surface [18,19]. However, a conflicting result in surface wettability has been reported [20]. In addition, heterogeneous material coating such as ZrC and ZrN on fuel cladding surface has been suggested as a promising method to reduce crud deposition due to increase of repulsive force in zeta potential [21].

In this work, we provide the mitigation methods of fuel crud deposition through the experimental observation for surface condition of fuel cladding on crud deposition [8,22,23]. The surface condition of Zr alloy fuel cladding was controlled through various methods such as pre-oxidation, chemical etching and crud-resistance coating. Crud deposition tests were performed to quantify the relative crud mass under a sub-cooled nucleate flow boiling condition occurring in a simulated primary water at 328°C using a circulating loop system. The obtained results are discussed in many surface properties.

2. Experimental methods

1.0Sn-1.0Nb-Zr alloy cladding tubes, which has the same properties with commercial Zirlo™ cladding, was utilized as the specimen. Table 1 shows the chemical composition and mechanical properties of the cladding tube used in this work. The cladding tube has the following dimensions; inner diameter(ID) of 8.3 mm, outer diameter(OD) of 9.5 mm, tube thickness of 0.57 mm, and length of 550 mm.

TABLE 1. Chemical composition and mechanical properties of 1.0Sn-1.0Nb-Zr alloy.

Composition (wt.%)					Mechanical properties (at RT)		
Sn	Fe	O	Nb	Zr	YS(MPa)	UTS(MPa)	Elong.(%)
1.0	0.1	0.1	1.0	Bal.	612.5	819.2	15.8

The surface condition of cladding tube was controlled by three methods as below;
— Chemical etching;
  • The chemically etched tube was prepared by immersing in an acid solution composed of 45 vol% nitric acid (65%-HNO_3), 5 vol% hydrofluoric acid (48%-HF), and 50 vol% deionized (DI) water for 3 min at room temperature. To prevent chemical etching of the inner surface, one end of the cladding tube was welded with a zirconium plug to provide a leak-tight joint. The cladding tube was immediately rinsed in DI water for 10 min using an ultrasonic cleaner to avoid staining of the surface with the residual etching chemicals.
— Preoxidation;
  • One end of the cladding tubes was welded with a zirconium plug to give a leak tight joint during crud deposition test. Two tubes were pre-oxidized at 400°C in the air of an electric chamber furnace for 3 days and 33 days, respectively. In this case, only the 25 cm long part from the closed tube end was heated in the furnace at 400°C, and the remaining part of the tube (the open end side of the tube) was located outside the furnace. To prevent the oxidation on the inner surface of the tube, a vacuum condition in inside of cladding tube was created by using rotary pump. The oxidized specimens were degreased in acetone and rinsed by DI water before the tests using an ultrasonic cleaner.
— Aluminium oxide coating;
  • Al_2O_3 layer was coated using atomic layer deposition (ALD) technique on the surface of the prepared tubular and flat segments. Specimens were prepared by cutting of long cladding tube into tubular segments with a length of 6 mm and small rectangle pieces of 3 mm x 5 mm. The OD surface of small rectangle piece was ground with silicon carbide (SiC) paper to have a flat surface to measure the wettability and surface zeta potential. At this time, the roughness of the flat surface was controlled to be the same as that of the as-received cladding tube. ALD of Al_2O_3 layer was conducted at 250°C with trimethylaluminum [$Al(CH_3)_3$, TMA] and DI water as reactants. One cycle of thermal ALD-Al_2O_3 growth consisted of a pulse of TMA, followed by a pulse of DI water. Each

step was carried by a flow of nitrogen gas and separated by purge time. Two processes were performed alternately 200 times.

The as-received, chemically-etched and preoxidized tube specimens were heated using a cartridge heater to provide the condition of SNB on the surface of the tube specimen during the crud deposition test as shown in Fig. 1(a). The gap between the cladding tube and the cartridge heater was filled with MgO paste. The ring specimens of as-received (uncoated) and Al_2O_3-coated segments were put on a cartridge heater as shown in Fig. 1(b). The diameter of the heater was designed to provide tight thermal contact with the ring specimens. As shown in Fig. 1(b), the six uncoated rings and six Al_2O_3-coated rings alternately were put on the heater rod. The all specimens were degreased in acetone, ethanol and DI water for each 10 min, respectively, using ultrasonic cleaner. The degreased specimens were finally dried with nitrogen gas and loaded to autoclave lid.
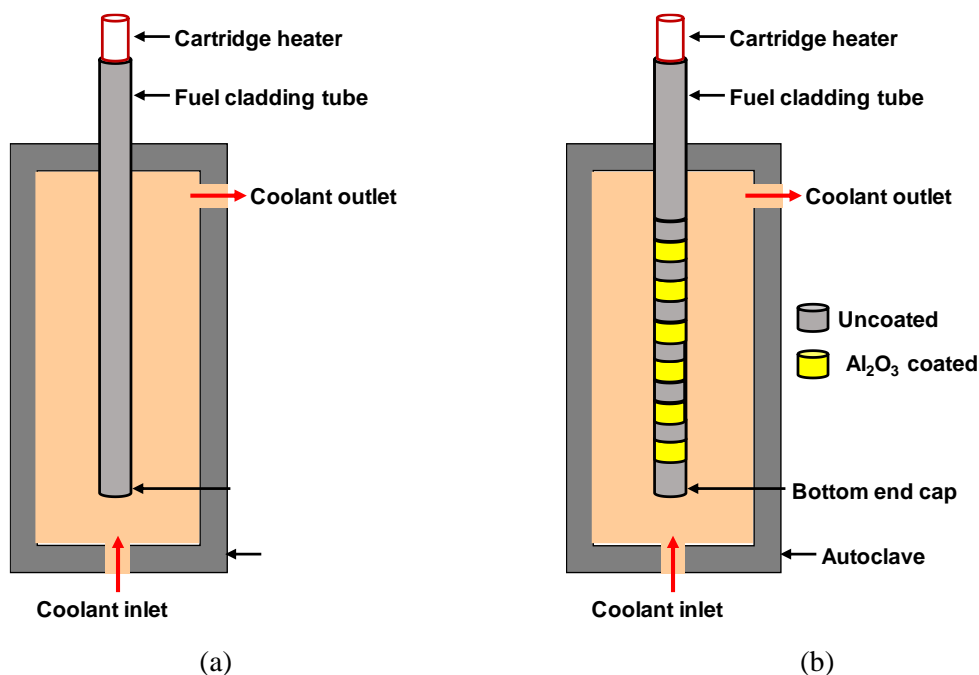

FIG. 1. Crud deposition samples; (a) As-received, chemically-etched and pre-oxidized tubes and (b) As-received and Al_2O_3-coated segments.

Test solution was prepared by dissolving 3.5 ppm Li (LiOH) and 1500 ppm B (H_3BO_3) into 200L DI water, which was used to simulate a PWR primary water. This solution of 200L was stored in the solution tank. The sources of Ni and Fe ions for crud deposition were prepared using Ni- and Fe-ethylenediaminetetraacetic acid (EDTA), respectively. The mixed source solution of 1,000 ppm Fe and 40 ppm Ni in weight was stored in the source tank for injection to the test section.

Crud deposition tests were performed in a STS 316L autoclave connected to a primary water recirculating loop system, which was shown in Fig. 2. The inlet solution into the test section was preheated and the temperature of the flowing water adjacent to the specimens was maintained at 328°C. The temperature of the internal cartridge heater was maintained at 380°C to provide the condition of SNB on the surface of the specimens during crud deposition tests. The temperature condition was confirmed in our previous study, which was performed to obtain the presence of active SNB through both acoustic emission and boiling chimney

observation. The pressure of the test section was regulated at 130 bars. Dissolved oxygen was controlled to be less than 5 ppb and dissolved hydrogen was maintained at 35 cc /kg·H_2O (STP) by controlling the hydrogen overpressure of the solution tank. The flow rate adjacent to the specimens in the test section was controlled at 0.5 m/sec. After all these conditions are stabilized, injecting the crud source solution containing the mixed Fe and Ni ions into the test section was started via the metering injection pump. The mixed precursor ions were injected with a flow rate of 1.1 ml/min from the injection tank directly to the downstream of the preheater. This precursor solution is diluted in the simulated primary water stream and then its final chemistry is calculated to be 4.0 ppm Fe and 0.16 ppm Ni in the test section. The deposition was performed in different condition for specimen type as summarized in Table 2.
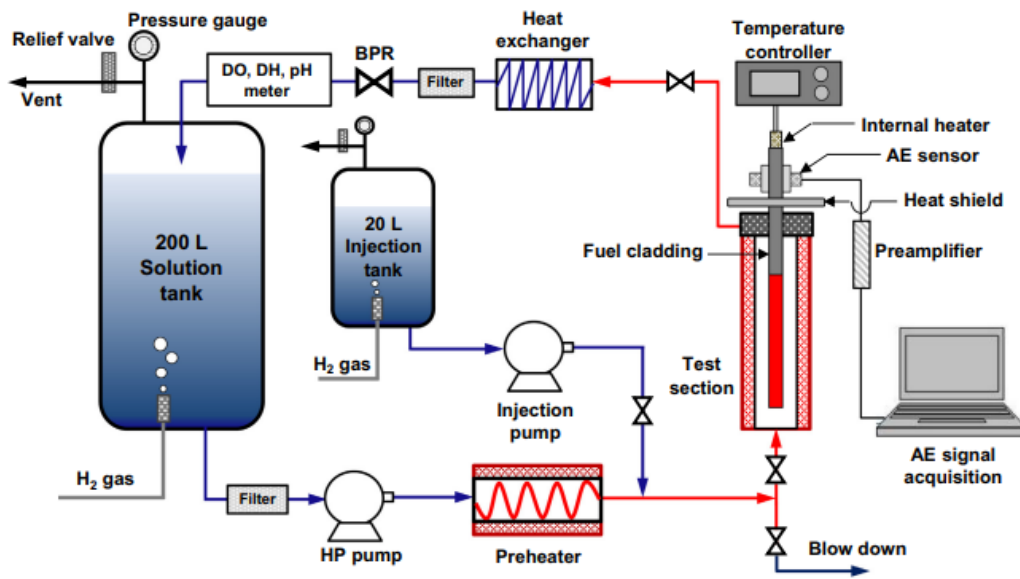

FIG. 2. Schematic of the test loop system for crud deposition.

TABLE 2. Experimental condition for the crud deposition test.

Test ID	Specimen	Temperature	Pressure	Solution in Test section	DO/DH	Test time
Chemical etching	As-received Chemically-etched	328ºC (380ºC)	13.0 MPa	1500ppm B 3.5ppm Li 3.93ppm Fe 0.16ppm Ni	DO<5ppb DH=35 cc/kg·H_2O	120h
Pre-oxidation	As-received 3d pre-oxidized 33d pre-oxidized					120h
Al_2O_3 coating	As-received Al_2O_3-coated					168h

The acoustic signals generated from the sub-cooled nucleate boiling on the heated cladding surface were monitored using the acoustic emission (AE) technique for 5 min every 24 h during the deposition tests. An AE sensor was directly coupled to the upper end of the cladding tube, as shown in Fig. 2. The AE sensor was connected to a pre-amplifier, which was connected to the AE signal acquisition system. A low frequency AE sensor (type R3a, 30–75 kHz resonant frequency, MISTRAS from Physical Acoustic Corporation, USA) was chosen to collect the AE-boiling signals. The obtained AE signals were analyzed using the AE-win software (Model: PCI-2, Physical Acoustic Corporation, USA).

To characterize the wettability and surface-corrosion particle interaction on prepared specimens, water contact angle and surface zeta potential were measured. After the deposition tests, the deposits on the surface of specimens were dissolved in aqua regia solution. At this time, the insides of the specimens were plugged by resin to analyse only the outside surface. Then, the concentrations of Ni and Fe were analyzed using an inductively coupled plasma – atomic emission spectroscopy (ICP-AES). To calculate the amount of the crud, the mass of Ni and Fe, determined by ICP-AES, was divided by the outside surface area of the specimens. The morphology of the crud was analyzed using a scanning electron microscope (SEM). The crud structure formed on the specimens was analyzed using X-ray diffraction equipment. The thickness of the coating was determined using focused ion beam (FIB) milling technique, and the chemical composition across the interface between crud and matrix was analyzed using an energy dispersive x-ray spectroscopy.

3. Results and discussion

3.1. Chemical etching effect

Fig.3 shows the topographical images and water contact angle measured on the surfaces of the a-received and chemically etched cladding tubes. The chemically etched surface was smoother over a wide region than the as-received surface as shown in Figs. 3(a) and 3(b). The surface roughness was measure 0.15µm on the as-received tube and 0.04 µm on the chemically-etched tube, respectively. The contact angles were measured as 77 ± 2° for the as-received surface and 39 ± 2° for the chemically etched surface, respectively. This result indicates that the chemically etched surface is a more hydrophobic than the as-received surface due to its smooth surface state.

Fig.4 presents the energy distribution of the AE signals acquired from both specimens for 500s every 24h during the crud deposition tests. In the beginning of test, the AE signals on the as-received cladding were detected mainly in the AE energy range below 500 aJ, whereas those on the chemically etched cladding were recorded in the low AE energy range below 200 aJ. In addition, the energy distribution of the AE signals on the as-received cladding expanded to higher energy levels below 2500 aJ with increasing test time, whereas the AE signals from the chemically etched cladding was constantly recorded in a lower range below 250aJ throughout the test. The energy of an AE signal means the strength of the acoustic sound emitting from a vapor bubble on the cladding surface. According to the reports on the correlation between vapor bubble size is proportional to the energy of the AE signal. However, the AE signals emitted from the fuel cladding surface included various boiling dynamics such as formation, growth, departure, collapse and collision along the axis of the cladding tube in the current work. The AE energy can be affected by not only the bubble size, but also the boiling dynamics mentioned above. Therefore, it is reasonable to consider that a relatively weak boiling dynamics such as reduction of bubble size and of boiling event frequency occurs on the chemically etched cladding. Furthermore, number of boiling events in AE signals appears extremely high on the as-received surface than on the chemically etched surface. This indicates that the boiling behaviour increased remarkably on the as-received cladding than on the chemically etched cladding during the deposition tests.

Fig. 5 shows the SEM micrographs of the deposits on the both cladding tubes after deposition tests. Polyhedral particles were uniformly deposited on both tubes. In addition, relatively small particles were also observed on both claddings. However, the size and density of the deposits were larger on the as-received cladding than on the chemically etched cladding. Furthermore,

boiling chimneys were formed on the as-received cladding as shown in Fig. 5(a), whereas no boiling chimney was observed on the chemically etched cladding as shown in Fig. 5(b).
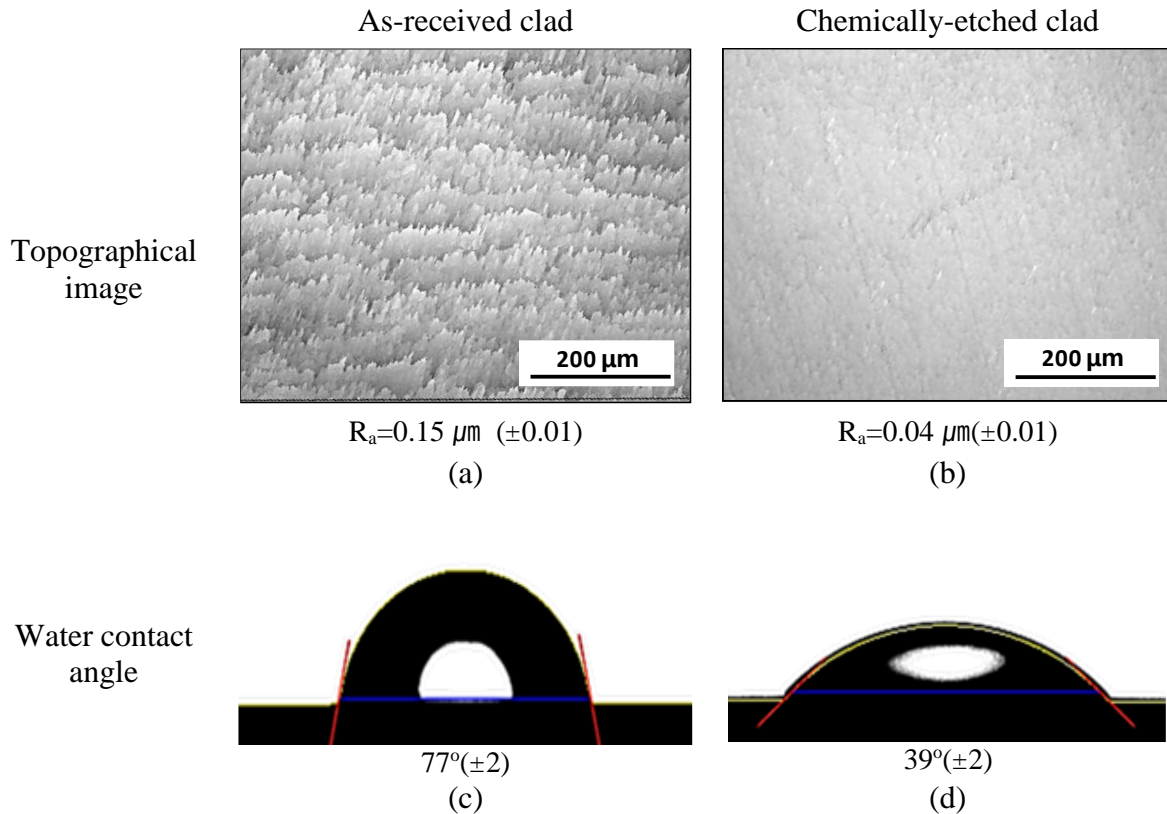
	As-received clad	Chemically-etched clad
Topographical image	$R_a=0.15\ \mu m\ (\pm 0.01)$ (a)	$R_a=0.04\ \mu m(\pm 0.01)$ (b)
Water contact angle	$77^o(\pm 2)$ (c)	$39^o(\pm 2)$ (d)

FIG. 3. Topographical images (a, b) and static contact angles of water droplets (c,d) on the specimens; (a) &(c) unetched clad, (b) & (d) chemically-etched clad.
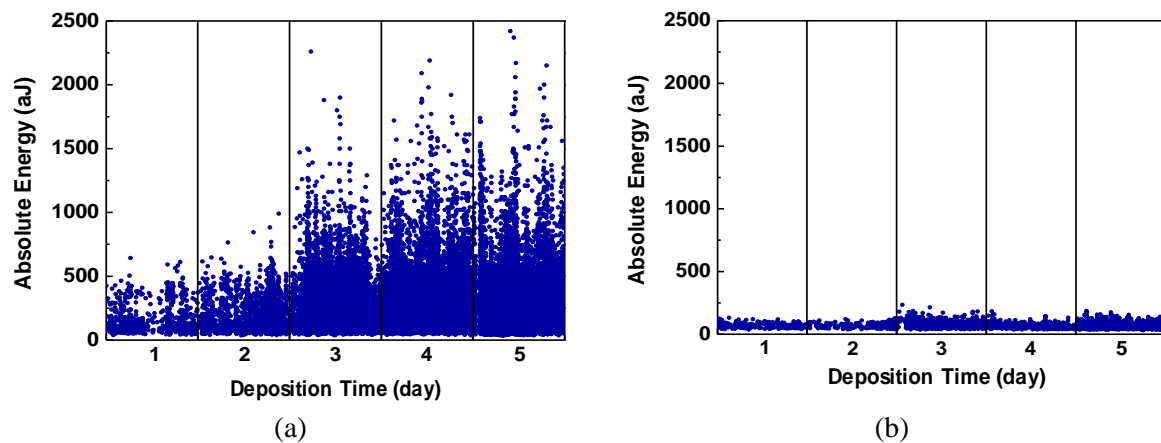
FIG.4. Distribution of energy of acoustic signals during the crud deposition tests; (a) as received cladding and (b) chemically etched cladding.

Fig. 6 shows the SEM images of the deposits before FIB machining, STEM images of the cross section of the machined deposits, and their elemental maps on the both cladding tubes. The yellow boxes in the SEM images of the deposits indicate the locations where the cross-sectional specimens were machined by using FIB. As shown in the elemental maps, the polyhedral particles as well as the relatively small particles are Fe oxides composed mainly of iron and oxygen. Additionally, STEM-EDS point analysis performed at the locations marked in the

STEM images revealed that deposits have a typical magnetite composition, as summarized in Table 3.
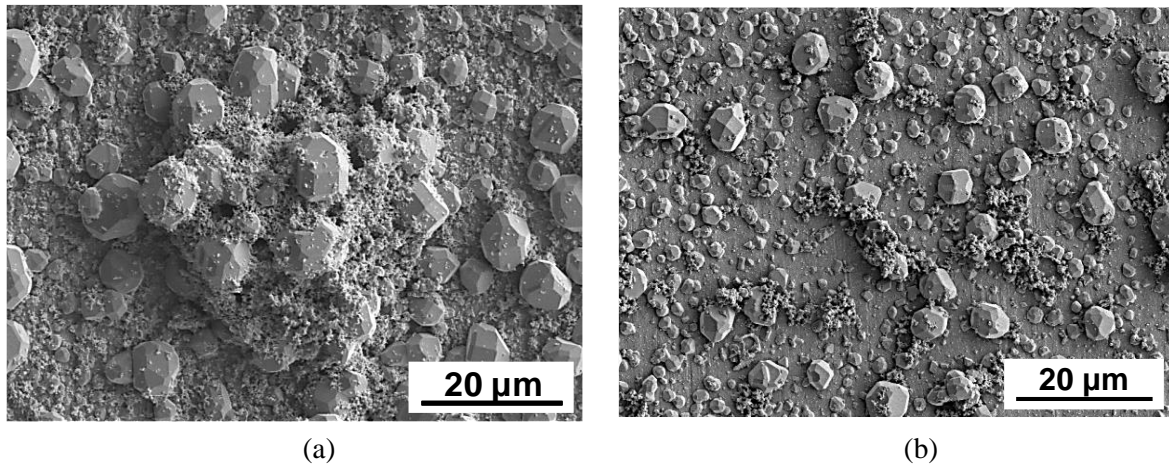

(a)   (b)

FIG.5. SEM micrographs of the deposits after deposition tests; (a) as received cladding and (b) chemically etched cladding.

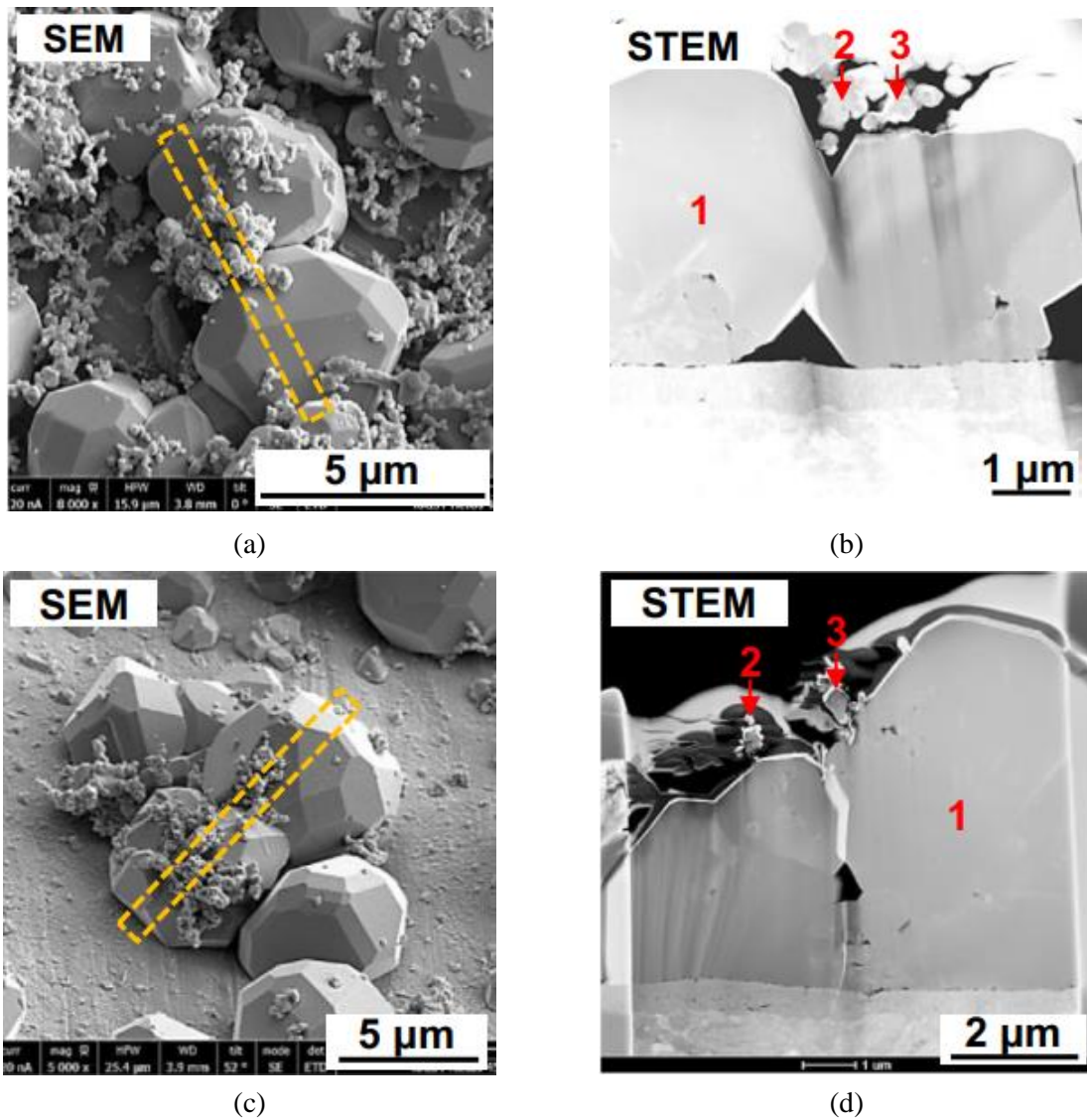(a)   (b)

(c)   (d)

FIG.6. SEM and STEM images of fuel deposits; (a, b) as-received cladding and (c,d) chemically etched cladding.

TABLE 3. Chemical compositions (at%) of the deposits measured by STEM-EDS point analysis at the locations marked in Figs. 6(b) and 6(d).

Cladding	Point	O	Fe	Ni	Zr
As-received	1	56.5	43.2	<0.2	0.2
	2	59.1	40.1	<0.1	0.8
	3	58.8	41.0	<0.1	0.2
Chemically-etched	1	55.6	44.0	<0.1	<0.1
	2	59.7	40.1	<0.1	<0.1
	3	58.4	41.3	<0.1	<0.1
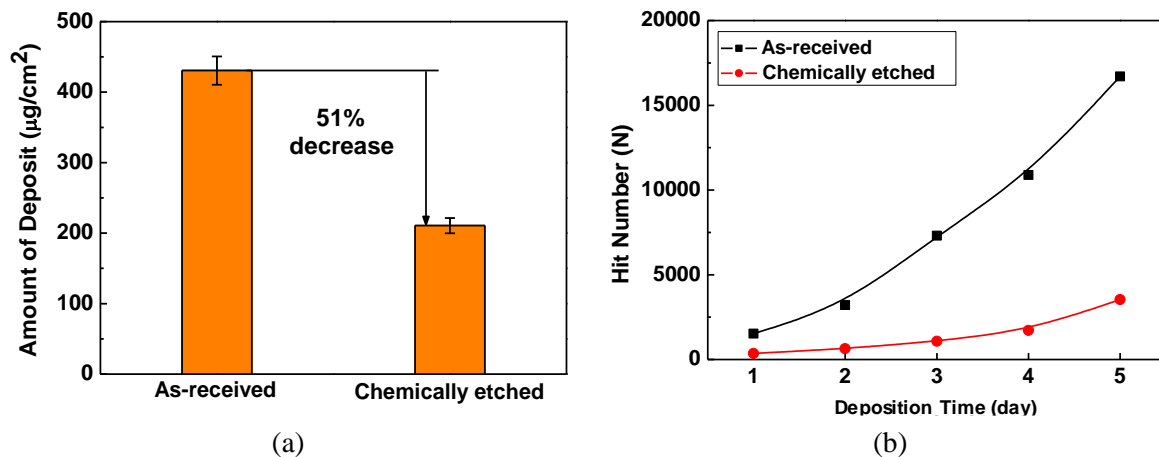
FIG.7. (a) Amount of deposits and (b) AE hit number on both claddings for 5 days.

Fig. 7 presents the crud amount deposited on both cladding tubes and AE hit number during deposition test. The mass of deposit decreased by 51% on the chemically etched cladding compared to that on the as-received cladding as shown in Fig. 7(a). This indicates that crud deposition was significantly dependent on the surface states of cladding tube. In addition, the mass of deposited crud strongly depends on the number of boiling events, which is caused by surface state. The hit number of the AE signals on both claddings increased with time during the crud deposition test as shown in Fig. 7(b). A number of hits on the as-received cladding was increased by 6-7 times than that of the chemically etched cladding tube.

The effect of chemical etching of the cladding tubes on the crud deposition behaviour can be discussed from the viewpoint of degree of SNB with changes in surface roughness and wettability. In the current work, the boiling behaviour can be affected by the following factors: temperature of the cladding surface, system pressure, coolant type, flow velocity, and cladding surface property. Although we could not measure the temperature of the cladding surface, the temperature of the internal heater, coolant fluid, system pressure, and flow velocity were maintained constant during the deposition runs. Therefore, it is reasonable to consider that the major factor affecting the boiling behaviour is the surface characteristics of the fuel cladding tubes. The change in surface characteristics by the chemical etching of the as-received cladding tube can be summarized as follows: the contact angle reduced by a factor of about 2, as shown in Fig. 3, respectively. The roughness of the fuel cladding surface can be affected by residual imperfections. However, the imperfections were removed through the chemical etching process and it should lead the reduction of surface roughness as well as the enhancement of surface wettability. In addition, the improvement in surface roughness and wettability should affect to

boiling heat transfer as shown in Fig. 7(b). It is well known that the nucleation and growth of bubbles is increased on the rougher surface. The difference in boiling behaviour for surface roughness has been explicated in our previous work, in which we demonstrated the visualization of boiling behaviour for different surface state. Therefore, it is considered that the crud deposition is accelerated by enhancement in heat transfer due to surface modification as shown Fig. 7(a).

3.2. Pre-oxidation effect

Fig. 8 shows the surface and cross-sectional SEM images of the pre-oxidized claddings. A uniform black oxide was formed on the pre-oxidized cladding at 400°C for 3 days, whereas partially white oxide with some radial cracks was observed on the pre-oxidized cladding at 400°C for 33 days as shown in Figs. 8(a) and 8(b). In this work, the as-received, 3 days pre-oxidized, and 33 days pre-oxidized cladding were compared in various characteristic assessments and named as AR, PO-3, and PO-33, respectively. The surface roughness measured was similar each other: 0.17μm for AR, 0.16μm for PO-3, 0.18μm for PO-33. Figs. 8(c) and 8(d) show the cross-sectional images of the pre-oxidized claddings machined by FIB. The oxide thickness was measured to be 0.71μm for PO-3 and 4.55μm for PO-33. These oxide layers were analysed to be zirconium oxide(ZrO_2) by XRD analysis. The oxide layer for PO-3 was uniformly grown over the sample surface and micro-cracks were rarely observed in the oxide layer. However, the thick oxide layer for PO-33 was observed with many short cracks approximately parallel to the matrix/oxide interface. However, the radial surface cracks propagated perpendicularly to the matrix/oxide interface. Some cracks seemed to be interconnected. These cracks are known to be formed by stresses due to the volume change from Zr to ZrO_2.

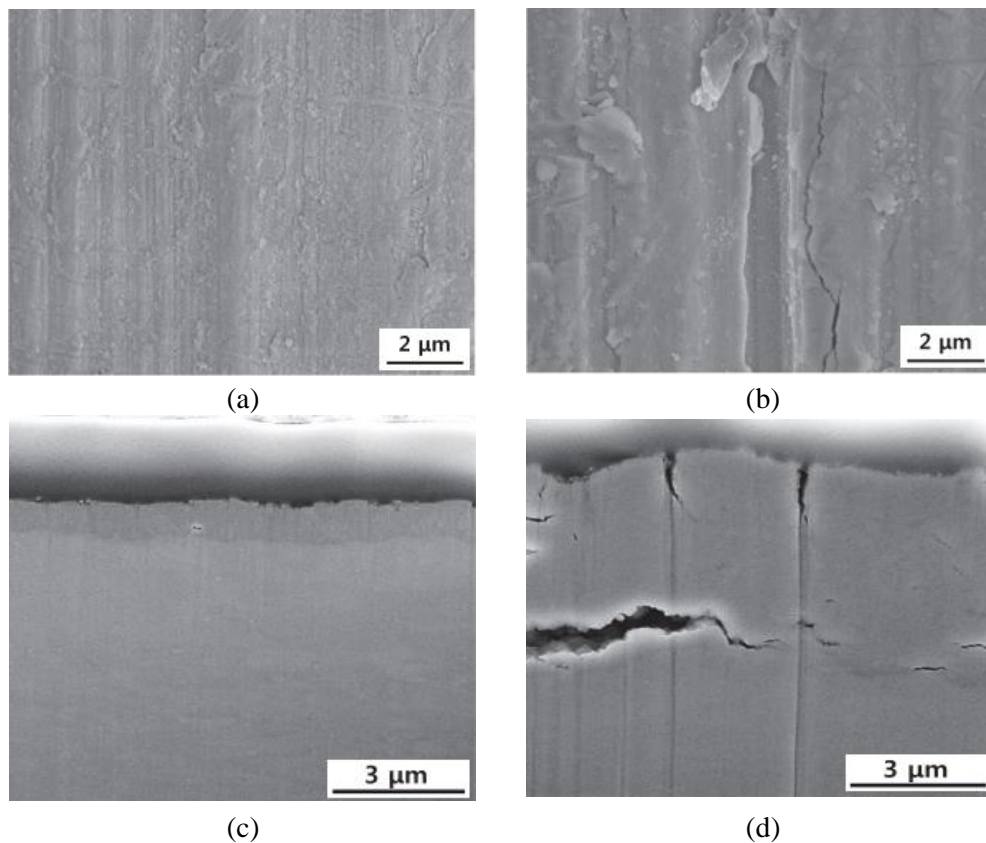| (a)	(b)

(c)	(d)

FIG.8. Surface and cross-sectional SEM images of pre-oxidized specimens; (a, c) PO-3 and (b,d) PO-33.

Fig. 9 shows the surface zeta potentials of the three different claddings and summarized in Table 4. The zeta potential of the magnetite (Fe$_3$O$_4$) nanoparticles was also superimposed in this figure. They were all negatively charged under the same test condition. The zeta potential of the Fe$_3$O$_4$ particles was measured to be -36.0 mV. The particles agglomerated together during dilution and stabilization, and thus the hydrodynamic average particle size was measured to be 78 nm by dynamic light scattering technique. The surface zeta potential of the as-received cladding was -43.5 mV. However, the surface zeta potentials of the pre-oxidized claddings decreased to -37.9 mV ~ -36.8 mV. This means that the repulsive forces between Fe$_3$O$_4$ particle and cladding surface are reduced as the cladding surfaces become oxidized to zirconium oxide.

The water contact angle on the surface of three specimens was measured as 72 ± 1° for AR, 66 ± 1° for PO-3 and 65 ± 1° for PO-33, respectively, as shown in Table 4. The thickness change of the pre-oxidized layers had no effect on the wettability. Hence, the static angle was slightly decreased by the pre-oxidized layer formed on the clean cladding surface. That is, the zirconium oxide surface has a slightly more hydrophilic property.
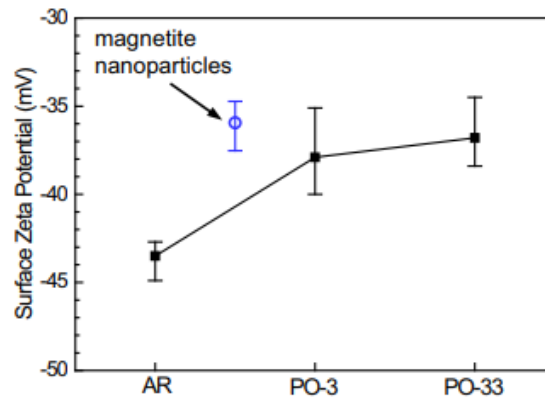

FIG.9. (a) Amount of deposits and (b) AE hit number on both claddings for 5 days.

TABLE 4. Surface zeta potential and water contact angle on the cladding specimens.

Specimen	Surface zeta potential (mV)	Potential difference (mV)	Contact angle(^{o})
AR	-43.5	7.5	72
PO-3	-37.9	1.9	66
PO-33	-36.8	0.8	65
Fe$_3$O$_4$ particle	-36.0 (Particle zeta potential)	0	-

Fig. 10 shows the SEM micrographs of the deposits on the three different cladding tubes after the deposition testes. Polyhedral particles were uniformly deposited on all kinds of specimens, but the density of the deposits became higher as the pre-oxidized layer was grown thicker. The boiling chimneys were also clearly observed on the cladding surfaces. These deposits were analyzed to be magnetite by XRD patterns, as shown in Fig. 11. The zirconium oxide peaks observed on the as-received cladding are attributed to the internally grown oxide during the deposition test.

Fig. 12 shows the deposit amount and AE hit number on the three different cladding tubes. The amount of deposits was heavily dependent on the surface states of the cladding. The deposit mass increased by 14 % for PO-3 and 45 % for PO-33, respectively, comparing to AR as shown in Fig. 12(a).
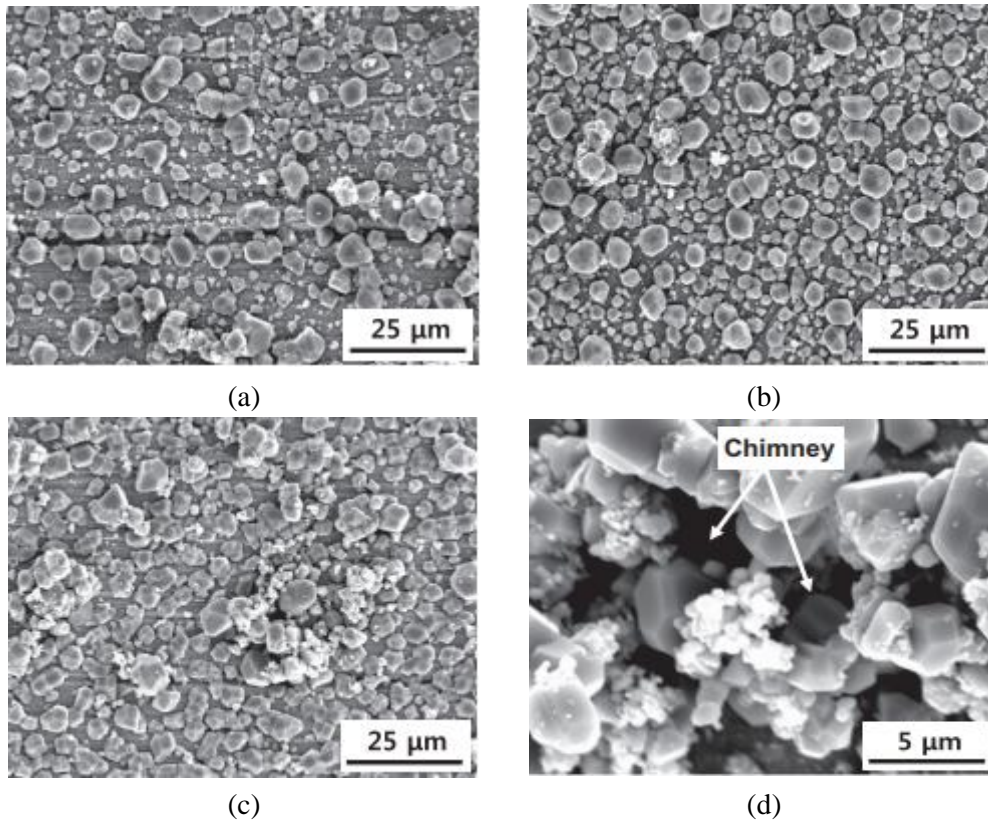

FIG.10. SEM micrographs of the deposits on the three different cladding tubes after the deposition tests: (a) AR, (b) PO-3, (c) PO-33, and (d) boiling chimneys observed in Fig. 10(c).
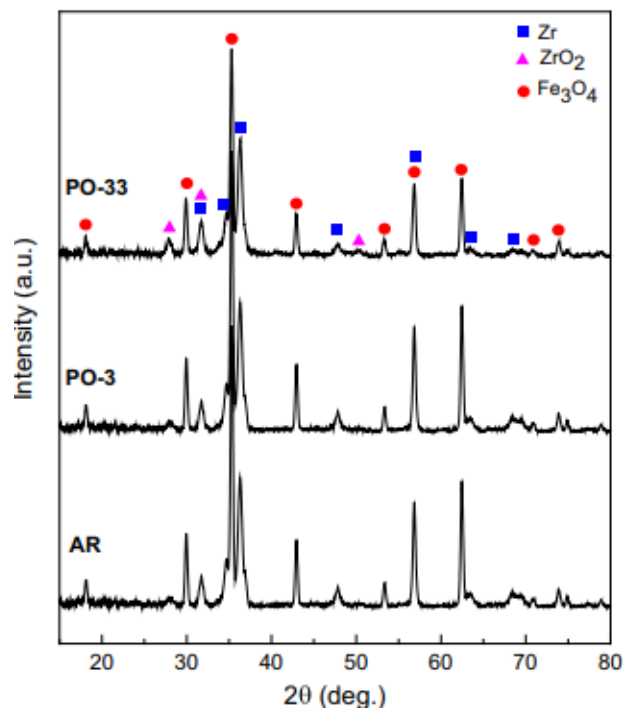

FIG.11. XRD patterns of the three different cladding tubes after the deposition tests.
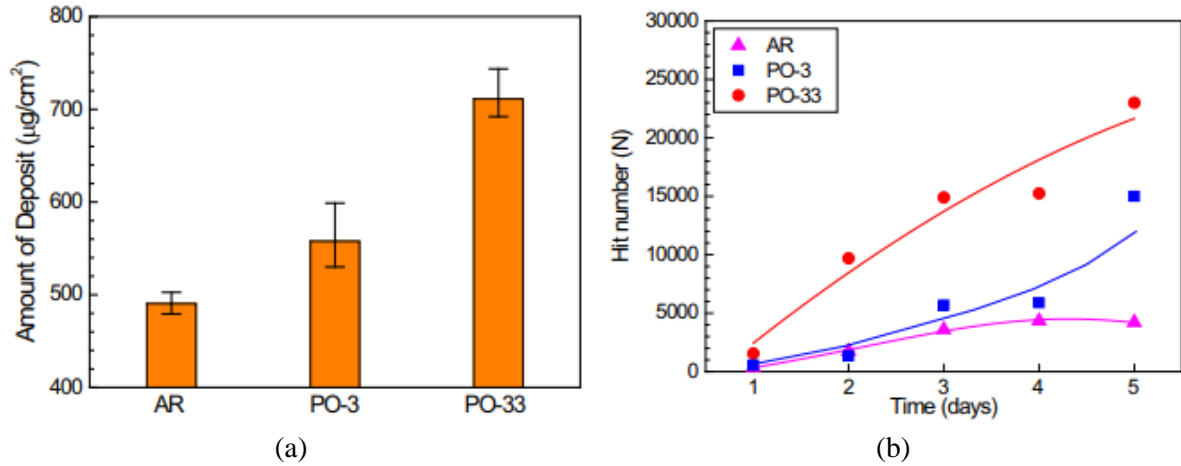
FIG.12. (a) Amount of deposits and (b) AE hit number on three different claddings for 5 days.

As shown in Fig. 12(b), the hit number of the boiling signals increased on a given cladding over time, and indicated also higher values on the cladding with a thicker pre-oxidized layer. In addition, the low energy signals below 500 aJ were mainly detected in the beginning of the test regardless of the surface states. However, the signals were expanded to the higher energy levels, and the density of signals was significantly increased with test time. This indicates that the bubble diameter and formation frequency is actively enhanced as time increases. Furthermore, these boiling behaviours become much more distinct on the pre-oxidized surfaces.

The effect of pre-oxidized surface layer on the crud deposition behaviour can be discussed from the following viewpoints: degree of SNB, zeta potential, and wettability. The thermal conductivity of zirconium alloys such as ZIRLO and Zircaloy-4 is approximately 11-12 W/mK at room temperature, whereas that of zirconium oxide (ZrO_2) has a wide range of 0.8-2.0 W/mK. The thermal conductivity of the crud was also estimated to have a very low value of 0.7-0.9 W/mK.

The reduction in the thermal conductivity of zirconium oxide and crud increases the temperature of the matrix/oxide interface, due to the increased thermal resistance. Furthermore, the temperature of the internal heater and the flowing water around the cladding tube was maintained constantly at 380ºC and 328ºC, respectively, during all deposition tests. Therefore, although we could not measure the temperatures of the cladding surfaces, it is reasonable to consider that the temperature of the matrix/oxide interface increases as the pre-oxidized layer of the cladding thickens. Therefore, the temperatures within the oxide would be higher than the bulk saturation temperature. As shown in Fig. 8, cracks are also developed in the oxide as the oxide layer grows. These pores and cracks can be filled with water, of which temperatures would exceed the boiling temperature there. Consequently, the formation of vapor bubbles becomes active. This process can be facilitated as the thickness of the oxide layer and crud increases. This means that the degree of SNB increases on the cladding surface with a thicker oxidized layer. Consequently, it is well established that the number of boiling signals increases on the thicker oxidized surface, as shown in Fig. 12(b). According to the micro-layer evaporation and dry-out model, the formation of deposits on the heated surface during nucleate boiling was due to the evaporation of a micro-layer of liquid beneath a bubble. Therefore, this change of the SNB behaviours seems to be a key factor of the increase in the crud amount on the pre-oxidized claddings. On the other hand, at a given surface state, it was observed that the number of boiling signals increased as the test time passed, as shown in Fig. 12(b). In this case, two factors can be considered: Deposits are accumulated on the cladding surface and the

internal oxidation of the cladding simultaneously makes the oxide layer thicker as the deposition test time passes. These two factors lead to increase the degree of SNB, resulting in an increase in the number of boiling signals. On the other hand, at a given surface state, it was observed that the number of boiling signals increased as the test time increased, as shown in Fig. 12(b). In this case, two factors can be considered: Deposits are accumulated on the cladding surface and the internal oxidation of the cladding simultaneously makes the oxide layer thicker as the deposition test time passes. These two factors lead to increase the degree of SNB, resulting in an increase in the number of boiling signals. Electrostatic forces have an important effect on the deposition behaviour of particles towards a surface. Therefore, the zeta potentials between Fe_3O_4 nanoparticles and the cladding surfaces seem to play an important role in the process of crud deposition on the fuel claddings. The zeta potential data indicate that the repulsive force between the Fe_3O_4 nanoparticle and cladding surface decreases as the cladding surface become oxidized to ZrO_2. Consequently, transportation and adhesion of Fe_3O_4 particles onto the pre-oxidized surfaces is favoured. The hydrophobicity is slightly higher on pre-oxidized surface than on as-received surface, but it is negligible. The oxide layer grown on Zircaloy-4 fuel cladding in an operating PWR changed from a uniform black oxide into a non-uniform white oxide when the oxide layer reached about 5–10 μm. In this work, the oxide was black and about 0.71 lm thick for the PO-3 tube, and partially white and about 4.55 μm thick for the PO-33 tube. Therefore, the as-received cladding specimens used in this work may stand for fresh fuel claddings and the pre-oxidized cladding specimens for once or twice burned fuel claddings in the core. Based on the results of this work, it is reasonable to conclude that the crud deposition is favoured on the fuel assemblies in PWRs operated at extended fuel cycles and high temperatures.

3.3. Al_2O_3 coating effect

Fig. 13 shows the TEM-EDS analysis results on the cross-section of the Al_2O_3-coated ring specimen, which was processed using FIB. It was observed that the Al_2O_3-coated layer was very dense and uniformly deposited on the cladding surface. The average thickness of the Al_2O_3 layer was measured to be 22 ± 2 nm. Zirconium oxide layer about 20 nm thick was also observed between the coated layer and cladding matrix, which may be formed during the ALD process. The atomic ratio of oxygen to aluminum in the coated layer was calculated to be near 1.5 from the EDS data. Furthermore, the TEM micrograph and FFT pattern revealed that the Al_2O_3-coated layer had an amorphous structure. Fig. 14 shows the surface zeta potentials and water contact angles of the uncoated and Al_2O_3-coated specimen. Both surfaces were all negatively charged under the same test condition. The surface zeta potential was approximately -43.5 mV for the uncoated specimen and -52.1 mV for the Al_2O_3-coated one as shown in Fig. 14(a). The zeta potential of the Fe_3O_4 nanoparticles themselves was also superimposed in this figure for comparison. The zeta potential of the magnetite particles was measured to be about -36.0 mV. The difference in the zeta potential between magnetite particle and cladding surface was larger on the coated surface than the uncoated one. This means that Al_2O_3 coating increases the repulsive forces between magnetite particle and Al_2O_3-coated surface. The contact angle was measured by 72±1° for uncoated surface and 85±1° for Al_2O_3-coated surface, respectively, as shown in Fig. 14(b). This indicates that the Al_2O_3 coating can provide a slightly more hydrophobic surface.

Fig. 15 displays the amount of crud deposits and zirconium oxide thickness on both the uncoated and Al_2O_3-coated specimens. The deposit mass decreased by about 23% for the Al_2O_3-coated specimens, comparing to the uncoated specimen as shown in Fig. 15(a). This

result indicates that crud deposition is dependent on the surface property of the cladding. In addition, the thickness of zirconium oxide layer grown during deposition test was thinner than that on the uncoated specimen, as shown in Fig. 15(b). This results shows the average thickness of zirconium oxide was reduced by about 12% by Al_2O_3 coating.

(a)

(b)

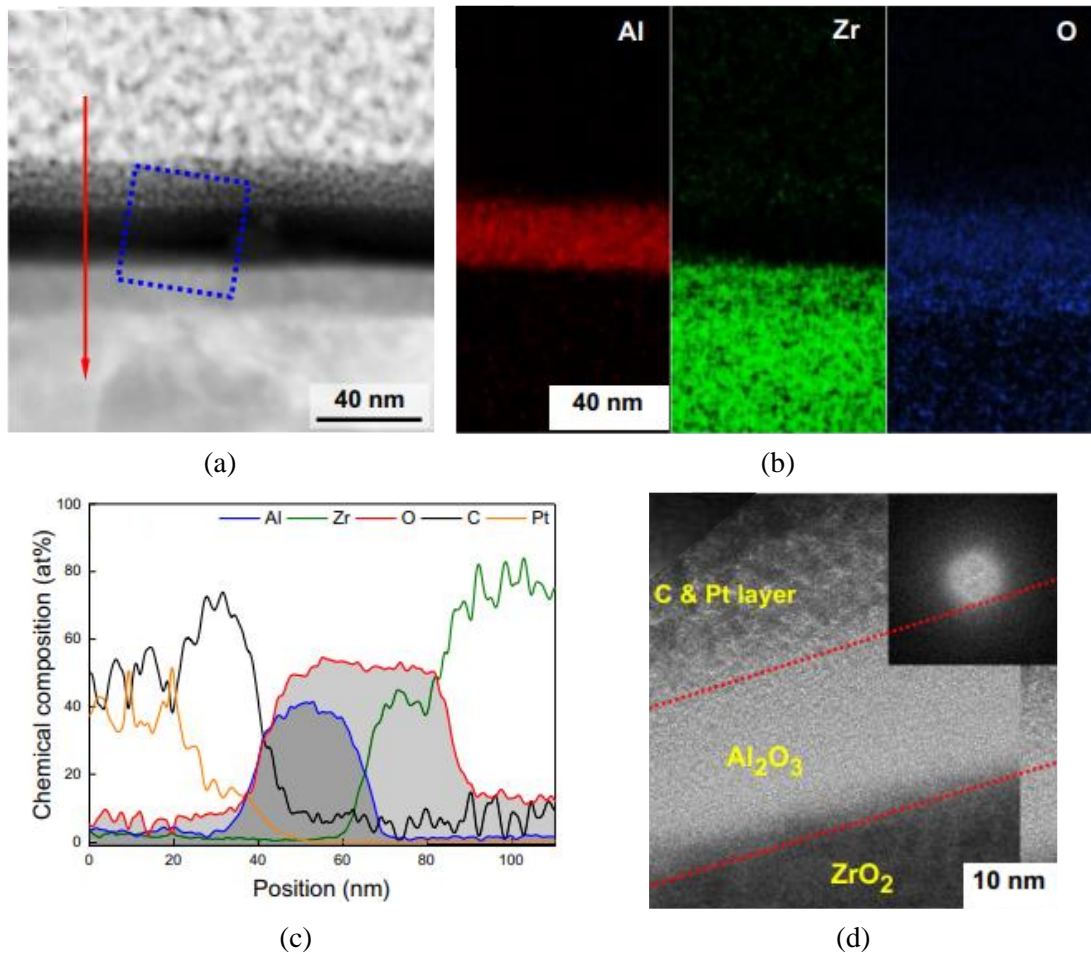(c)

(d)

FIG.13. TEM-EDS analysis of the Al_2O_3-coated cladding: (a) dark field scanning TEM image, (b) elemental mapping images, (c) EDS line profile (red arrow) and (d) TEM micrograph (dotted blue box). The inset in Fig. 13(d) is a FFT image on the Al_2O_3 layer.

(a)

(b)

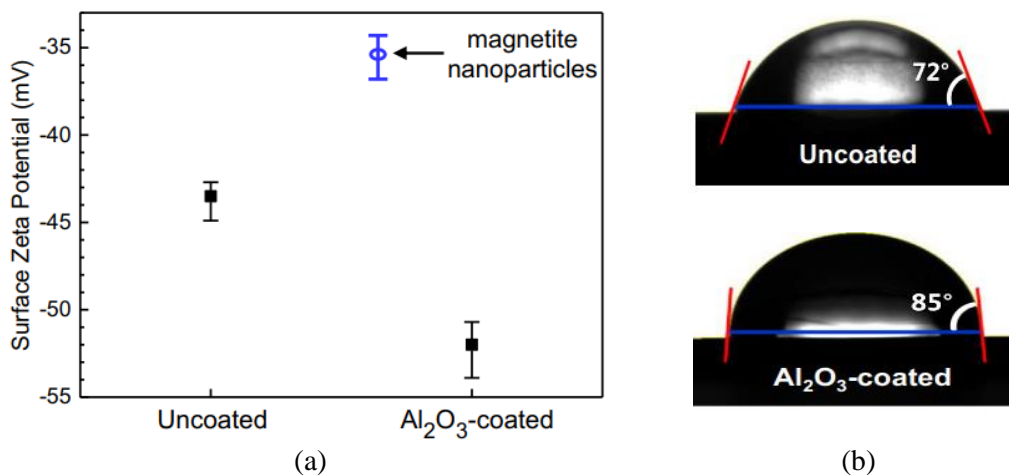*FIG.14. (a) Surface zeta potentials and (b) static contact angles of water droplets on the uncoated and Al_2O_3-coated claddings.*
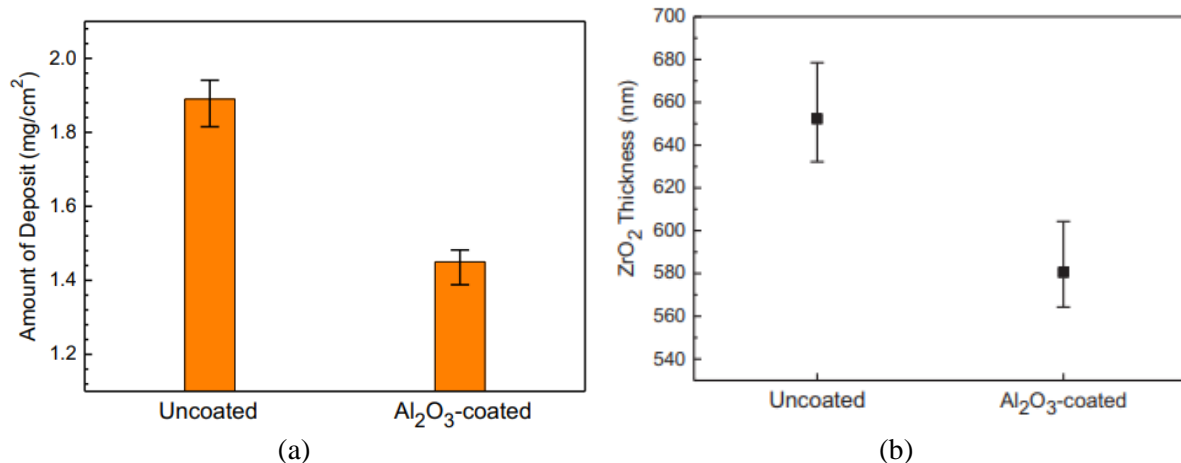
FIG.15. (a) Amount of crud deposits and (b) zirconium oxide thickness on both the uncoated and Al₂O₃-coated specimens.

Detailed chemical information near the interface between the crud and zirconium oxide could not be obtained from the SEM-EDS analysis. Therefore, TEM specimens were made using FIB machining, Fig. 16 shows the cross-sectional image of the Al_2O_3 coated specimen at high magnification. EDS line profile was performed to obtain chemical composition along the line a-b. The profile indicate that the upper bright part is Fe_3O_4 crud and the lower dark part is zirconium oxide. It is striking that Al_2O_3 was not detected in this region.
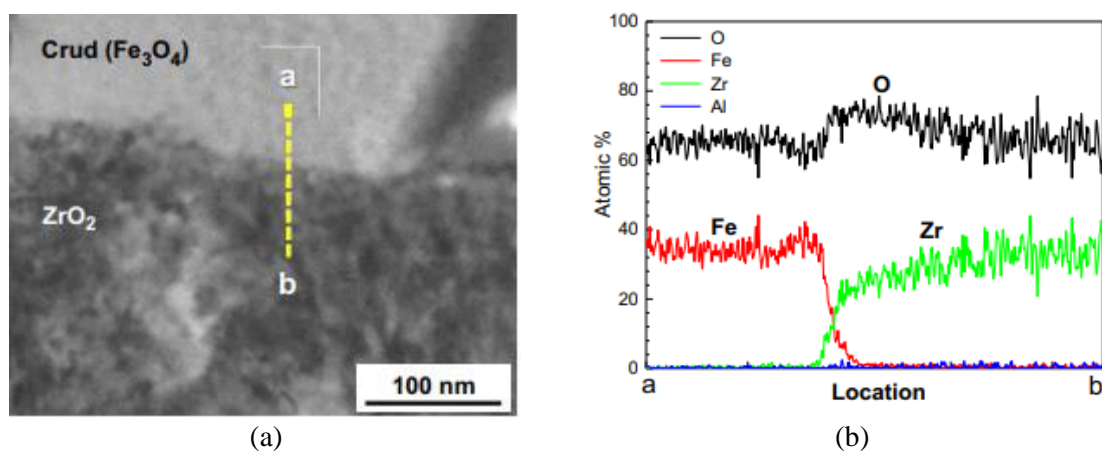

FIG.15. (a) TEM image on the cross-section of the Al₂O₃-coated cladding and (b) EDS profile along the line a-b..

The main findings in this work are as follows: the amount of crud was decreased by 23% through applying Al_2O_3 coating, whereas the coated Al_2O_3 layer disappeared after the deposition tests. First, a reduction of crud deposition due to Al_2O_3 coating can be discussed from surface properties such as zeta potential and wettability. Electrostatic forces have an important effect on the deposition behaviour of particle s toward a cladding surface. Therefore, the zeta potential between the corrosion product particle and cladding surface seems to play an important role in the process of crud deposition on the fuel claddings. As shown in Fig. 14(a), the difference of zeta potentials between Fe_3O_4 particle and cladding surface increased from 7.5 mV to 16.1 mV, when the cladding surface was coated by Al_2O_3 thin layer. Consequently, transportation and adhesion of Fe_3O_4 particles onto the Al_2O_3-coated surface is disfavoured, resulting decrease in crud deposition. The contact angle was increased from 72° to 85° by Al_2O_3

coating as shown in Fig. 14(b). This means that the Al_2O_3-coated surface has a slightly more hydrophobic property. According to the micro-layer evaporation and dry-out model, the formation of deposits on a heated surface during nucleate boiling was done by the escape of bubbles from the surface. Therefore, it is seen that the change in surface characteristics such as surface zeta potential and wettability affects to the boiling properties due to Al_2O_3 coating. However, the EDS line profiles indicate that the thermal/chemical stability of Al_2O_3 is very weak in the PWR primary coolant. Thus, it is considered that the Al_2O_3-coated layer plays a role to mitigate the crud deposition in early stage, but these function gradually weakened as the coated layer is dissolved. As the results, the corrosion resistance coating is very effective to reduce the crud deposition on fuel cladding but it can be seen that the chemical stability of coating material must be assessed in PWR primary condition prior to use.

4. Conclusions

We have investigated in this work that the effect of chemical etching, pre-oxidation, and Al_2O_3 coating on fuel crud deposition. In particular, the effect for crud deposition was measured and discussed in the viewpoint of the degradation of boiling behaviour and the decrease in corrosion product particle-cladding surface interaction. The main conclusions drawn are as follows:

(a) The amount of deposit on the chemically etched cladding decreased by about 51% compared to that on the as-received cladding due to the enhancement of heat transfer, and reduction in roughness and water contact angle.
(b) The amount of deposit on the pre-oxidized claddings increased as the pre-oxidized layer was thickened, especially by 45% compared with that on the as-received cladding. This can be caused by decrease in zeta potential difference between cladding surface and corrosion product particles, and increase in boiling events due to formation of oxidation layer.
(c) The crud deposition decreased by 23% through coating Al_2O_3 thin layer on fuel cladding. Furthermore, the Al_2O_3 coating leads to reduction in oxidation rate of zirconium alloy by 12%. It is seen that the decrease in crud deposition is also caused by increase in zeta potential difference and hydrophobicity. However, new coating materials will have to be searched due to the thermodynamic instability of Al_2O_3 in PWR primary water.

The surface modification techniques such as chemical etching and resistance material coating on fuel cladding is very useful method for mitigating crud deposition, but the pre-oxidation was a method to accelerate it. Therefore, the simulation tests for crud deposition with analysing surface characteristics performed in this work will provide a promising mitigation method for crud deposition to secure fuel integrity.

Acknowledgement

REFERENCES

[1] Sawicki, J.A., Evidence of Ni_2FeBO_5 and m-ZrO_2 precipitates in fuel rod deposits in AOA-affected high boiling duty PWR core, J. Nucl. Mater. 374(2008), 248– 269.
[2] Yeon, J.W., Choi, I.K., Park, K.K., Kwon, H.M., Song, K., Chemical analysis of fuel crud obtained from Korean nuclear power plants, J. Nucl. Mater. 404(2010), 160–164.

[3]   EPRI, PWR Axial Offset Anomaly (AOA) Guidelines, Rev. 1, EPRI Report 1008102, Palo Alto, CA, USA, 2004.

[4]   IAEA, Optimization of water chemistry to ensure reliable water reactor fuel performance at high burnup and in ageing plant. IAEA-TECDOC-1666, IAEA, Vienna, 2011.

[5]   Rák, Zs, Bucholz, E.W., Brenner, D.W., Defect formation in aqueous environment: theoretical assessment of boron incorporation in nickel ferrite under conditions of an operating pressurized-water nuclear reactor (PWR), J. Nucl. Mater. 461(2015), 350–356.

[6]   Cox, B., Some thoughts on the mechanisms of in-reactor corrosion of zirconium alloys, J. Nucl. Mater. 336(2005), 331–368.

[7]   Edsinger, K., Stanek, C.R., Wirth, B.D., Light water reactor fuel performance: current status, challenges, and future high fidelity modelling, J. Miner. Met. Mater. Soc. 63 (2011), 49–52.

[8]   Park, M.S., Shim, H.S., Baek, S.H., Kim, J.G., Hur, D.H., Effects of oxidation states of fuel cladding surface on crud deposition in simulated primary water of PWRs, Ann. Nucl. Energy 103(2017), 275-281.

[9]   Stevens, J., Farnsworth, D., Bosma, J., Deshon, J., Elevated RCS pH program at Comanche Peak, Proc. Int. Conf. on Water Chemistry of Nuclear Reactor Systems, Jeju, Korea, 2006.

[10]   EPRI, Pressurized Water Reactor Primary Water Chemistry Guidelines, Vol. 1, Rev. 7, EPRI Report 3002000505, Palo Alto, CA, USA, 2014.

[11]   Yang, R., Cheng, B., Deshon, J., Edsinger, K., Ozer, O., Fuel R & D to improve fuel reliability, J. Nucl. Sci. Technol. 43 (2006), 951–959.

[12]   Deshon, J., Edsinger, K., Frattini, P., Hussey D. and Wood, C.J., Ultrasonic fuel cleaning in PWRs and BWRs, Proc. Int. Conf. on Water Chemistry of Nuclear Reactor Systems, Jeju, Korea, 2006.

[13]   Iwahori, T., Mizuno, T., Koyama, H., Role of surface chemistry in crud deposition on heat transfer surface, Corrosion NACE 35(1979), 345–350.

[14]   Ferrer, A., Dacquait, F., Gall, B., Ranchoux, G., Riot, G., Modelling of crud growth phenomena on PWR fuel rods under nucleate boiling conditions, Proc. Int. Conf. on Water Chemistry of Nuclear Reactor Systems, Paris, 2012.

[15]   Jones, B.J., McHale, J.P., Garimella, S.V., The influence of surface roughness on nucleate pool boiling heat transfer, J. Heat Transf. 131(2009), 121009.

[16]   Alam, T., Lee, P.S., Yap, C.R., Effects of surface roughness on flow boiling in silicon microgap heat sinks, Int. J. Heat Mass Transf. 64(2013), 28–41.

[17]   McHale, J.P., Garimella, S.V., Bubble nucleation characteristics in pool boiling of a wetting liquid on smooth and rough surfaces, Int. J. Multiph. Flow 36(2010), 249– 260.

[18]   Cheedarala, R.K., Park, E., Kong, K., Park, Y.B., Park, H.W., Experimental study on critical heat flux of highly efficient soft hydrophilic CuO-chitosan nanofluid templates, Int. J. Heat Mass Transf. 100(2016), 396–406.

[19]   Yang, L.X., Chao, Y.M., Jia, L., Li, C.B., Wettability and boiling heat transfer study of black silicon surface produced using the plasma immersion ion implantation method, Appl. Thermal Eng. 99(2016), 253–261.

[20]   Phan, H.T., Caney, N., Marty, P., Colasson, S., Gavillet, J., Surface wettability control by nanocoating: The effects on pool boiling heat transfer and nucleation mechanism, Int. J. Heat Mass Transf. 52(2009), 5459–5471.

[21]   Dumnernchanvanit, I., Zhang, N.Q., Robertson, S., Delmore, A., Carlson, M.B., Hussey, D., Short, M.P., Initial experimental evaluation of crud-resistant materials for light water reactors, J. Nucl. Mater. 498(2018), 1–8.

[22]   Shim, H.-S., Park, M.-S., Baek, S. H., Hur, D. H., Effect of aluminium oxide coated on fuel cladding surface on crud deposition in simulated PWR primary water, Ann. Nucl. Energy 121(2018), 607-614.

[23]   Baek, S. H., Shim, H.-S., Kim, J. G., Hur, D. H., Effect of chemical etching of fuel cladding surface on crud deposition behaviour in simulated primary water of PWRs at 328ºC, Ann. Nucl. Energy 116(2018), 69-77.